

Non-Equilibrium Bose–Einstein Condensation of Exciton-Polaritons in Silicon Metasurfaces

Citation for published version (APA):

Castellanos, G. W., Ramezani, M., Murai, S., & Gómez Rivas, J. (2023). Non-Equilibrium Bose–Einstein Condensation of Exciton-Polaritons in Silicon Metasurfaces. *Advanced Optical Materials*, 11(7), Article 2202305. <https://doi.org/10.1002/adom.202202305>

Document license:

CC BY

DOI:

[10.1002/adom.202202305](https://doi.org/10.1002/adom.202202305)

Document status and date:

Published: 04/04/2023

Document Version:

Publisher's PDF, also known as Version of Record (includes final page, issue and volume numbers)

Please check the document version of this publication:

- A submitted manuscript is the version of the article upon submission and before peer-review. There can be important differences between the submitted version and the official published version of record. People interested in the research are advised to contact the author for the final version of the publication, or visit the DOI to the publisher's website.
- The final author version and the galley proof are versions of the publication after peer review.
- The final published version features the final layout of the paper including the volume, issue and page numbers.

[Link to publication](#)

General rights

Copyright and moral rights for the publications made accessible in the public portal are retained by the authors and/or other copyright owners and it is a condition of accessing publications that users recognise and abide by the legal requirements associated with these rights.

- Users may download and print one copy of any publication from the public portal for the purpose of private study or research.
- You may not further distribute the material or use it for any profit-making activity or commercial gain
- You may freely distribute the URL identifying the publication in the public portal.

If the publication is distributed under the terms of Article 25fa of the Dutch Copyright Act, indicated by the "Taverne" license above, please follow below link for the End User Agreement:

www.tue.nl/taverne

Take down policy

If you believe that this document breaches copyright please contact us at:

openaccess@tue.nl

providing details and we will investigate your claim.

The Current State of Reconstruction Technologies for 3D X-ray Microscopy including Algorithmic Innovation for AI-based Recovery

April 26, 10:00am - 11:00am EDT

Many properties can only be fully understood in 3D, such as porosity and tortuosity in porous materials, network connection maps in neuroscience, or mechanical properties in 3D additively manufactured structures. X-ray microscopy provides a unique method to image samples non-destructively in 3D across a wide range of materials and life sciences.

Watch this session during the WAS Virtual Conference:



Nicolas Guenichault, Ph.D.



Dr. Stephen T. Kelly, Ph.D.

[Register Now](#)

This talk is sponsored by



Non-Equilibrium Bose–Einstein Condensation of Exciton-Polaritons in Silicon Metasurfaces

Gabriel W. Castellanos,* Mohammad Ramezani, Shunsuke Murai,
and Jaime Gómez Rivas*

Exciton-polaritons (EPs) are hybrid light–matter quasi-particles with bosonic character formed by the strong coupling between excitons in matter and photons in optical cavities. Their hybrid character offers promising prospects for the realization of non-equilibrium Bose–Einstein condensates (BECs), and room-temperature BECs are possible with organic materials. However, the thresholds required to create BECs of organic EPs remain still high to allow condensation with electrical injection of carriers. One of the factors behind these high thresholds is the very short cavity lifetimes, leading to a fast EP decay and the need to inject higher exciton densities in the reservoir to form the condensate. Here a BEC of EPs in organic dyes and all-dielectric metasurfaces at room temperature is demonstrated. By using dielectric metasurfaces that exhibit very low losses it is possible to achieve cavity lifetimes long enough to allow an efficient population of EP states via vibrational relaxation and radiative pumping. It is shown how polariton lasing or non-equilibrium Bose–Einstein condensation is achieved in several cavities, and one of the lowest reported thresholds for BECs in organic materials is observed.

occupation of the ground energy state, which leads to macroscopic coherent quantum phenomena, such as enhanced non-linearities, superfluidity, and lasing without the need of population inversion.^[2,3] These phenomena encourage potential applications for BECs, such as ultra-low threshold polariton lasing,^[4,5] and quantum simulators.^[6] Polariton BECs of organic EPs have attracted tremendous attention in the last decade.^[5,7–10] Compared to most inorganic semiconductors, the large binding energies of Frenkel excitons in organics make possible condensation at room temperature. In addition, solution processing makes relatively easy the fabrication of organic devices. However, the realization of organic-polariton BEC devices remains elusive due to the high EP densities required to achieve the condensation threshold.

To move toward viable devices, these thresholds should be reduced from the current values of a few tens of $\mu\text{J cm}^{-2}$ to tents or hundreds of nJ cm^{-2} , which will allow electrical pumping. The reason behind these high thresholds lies in the inefficient population of the EP states. The buildup of a population of EPs is a process in which two mechanisms compete with each other: 1) the relaxation of excitons in the reservoir toward the ground state; and (2) the loss of photons from the cavity. While the first mechanism leads to the buildup of the EP population, the cavity losses reduce this population. If the loss rate of the cavity is faster than the relaxation rate of the exciton reservoir, a higher density of excitons have to be injected to form a condensate; therefore, increasing the threshold. Consequently, engineering the losses of the cavity would provide a path to reduce the BEC thresholds.


The typical cavities used for EP condensation suffer from important limitations: Fabry–Perot microcavities exhibit low or no optical absorption. However, it is difficult to engineer the radiative losses. Hemispherical microcavities allow for high Q -factors,^[11] but the complexity of their fabrication makes them less suitable for devices. Plasmonic metasurface cavities using metallic nanoparticles allow to control the radiative losses, but they are fundamentally limited by the high absorption of metals due to Ohmic losses.^[9,12] On the other hand, all-dielectric metasurfaces offer the unique possibility of reducing both absorption and radiative losses. Mie resonances in dielectric particles are much less dissipative than plasmonic

1. Introduction

Polariton Bose–Einstein condensates (BECs) are non-equilibrium condensates formed by exciton-polaritons (EPs), hybrid light–matter bosonic quasi-particles, originating from the strong coupling between excitons in matter and cavity photons.^[1] BECs are characterized by the bosonic collective

G. W. Castellanos, M. Ramezani, J. Gómez Rivas
Department of Applied Physics and Science Education
Eindhoven Hendrik Casimir Institute and Institute for
Complex Molecular Systems
Eindhoven University of Technology
P.O. Box 513, 5600 MB Eindhoven, The Netherlands
E-mail: g.w.castellanos.gonzalez@tue.nl; j.gomez.rivas@tue.nl

S. Murai
Department of Material Chemistry
Graduate School of Engineering
Kyoto University
Nishikyo-ku, Kyoto 615-8510, Japan

 The ORCID identification number(s) for the author(s) of this article can be found under <https://doi.org/10.1002/adom.202202305>.

© 2023 The Authors. Advanced Optical Materials published by Wiley-VCH GmbH. This is an open access article under the terms of the Creative Commons Attribution License, which permits use, distribution and reproduction in any medium, provided the original work is properly cited.

DOI: 10.1002/adom.202202305

resonances due to the much lower (or lack of) material losses. Furthermore, the engineering of Mie resonances can produce either high Q -factor modes,^[13,14] or even the total suppression of radiative losses through the so-called bound states in the continuum.^[15–17] This concept has been already explored in ref. [9], where Al nanoparticle arrays supporting dark plasmon modes resulted in the first demonstration of a polariton laser in a plasmonic cavity. Although the condensation threshold in this system is among the lowest reported, the high losses of metals make it impossible to reduce it further. Recent work has shown the potential of dielectric metasurfaces to modify the emission of weakly coupled emitters,^[18–22] and to achieve conventional lasing with remarkable low thresholds.^[23–28] The first step toward a non-equilibrium EP BEC is the strong coupling between excitons and the optical modes supported by dielectric metasurfaces, as it has been demonstrated recently.^[29–31]

In this manuscript, we demonstrate the first organic-polariton BEC at room temperature in an all-dielectric metasurface consisting of silicon nanoparticles. By exploiting in-plane diffraction orders, the metasurface is designed to support Mie surface lattice resonances (Mie-SLRs). Mie-SLRs can exhibit high Q -factor, resulting in a cavity that has simultaneously low radiative and low absorption/material losses. These characteristics have two important consequences in the EP dynamics that determine the threshold for condensation. First, through the lower losses,

that is, longer EP lifetimes, a lower density of excitons in the reservoir is needed to achieve condensation. Second, the suppression of losses opens the path to a radiative channel for exciton-polariton relaxation, allowing excitons that decay radiatively to efficiently increase the EP population. These two effects play out positively to reduce the threshold of condensation. Furthermore, radiative pumping is a relaxation mechanism that depends on the broad emission spectrum of the dye, and this allows to tune the condensation energy of the array with the periodicity. Dielectric scatterers have not yet attracted a lot of attention in the strong coupling regime of light–matter interaction due to the weaker field confinements as compared with plasmonic cavities. Yet, they offer a great potential due to the possibility of realizing lossless cavities. Building on our experimental results, we model the polariton dynamics and explore the potential that near-lossless cavities could bring into BEC.

2. Results

2.1. Strong Coupling between a Dielectric Metasurface and an Organic Dye

The cavity used in this study is shown schematically in Figure 1a and consists of periodic square arrays of silicon (Si)

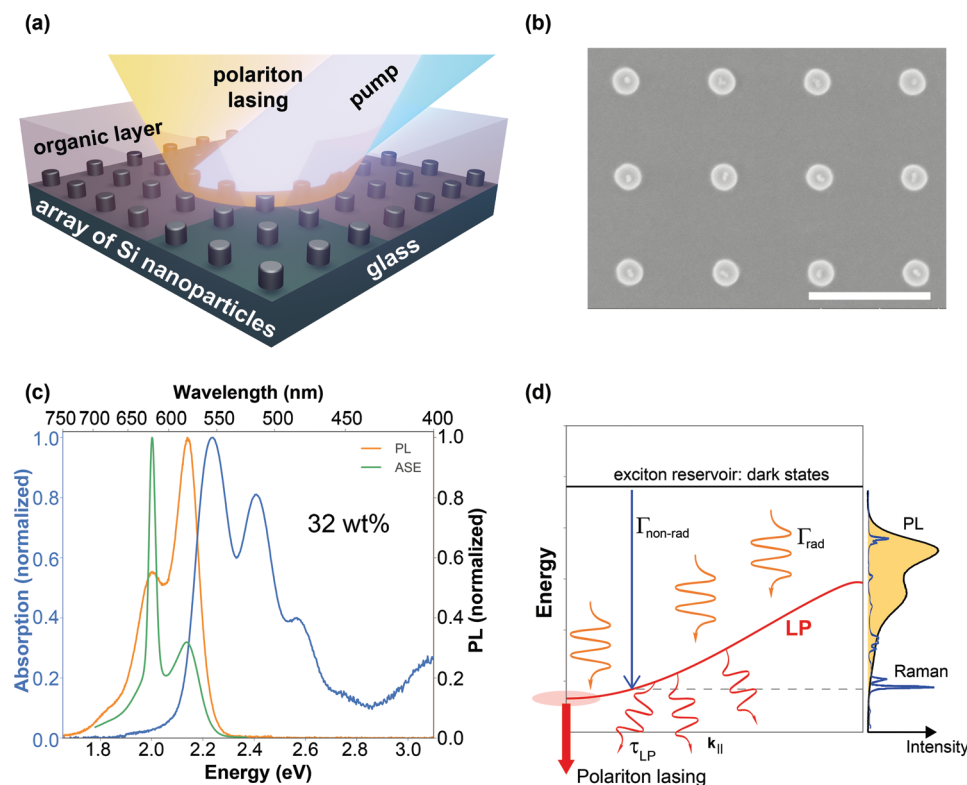


Figure 1. a) Schematic illustration of the metasurface cavity: an array of silicon nanoparticles on a substrate with a layer on top that contains the dye responsible of the BEC. b) An SEM image of one of the arrays. The horizontal bar represents a length of 500 nm. c) Absorption (in blue), photoluminescence (in orange), and amplified spontaneous emission (ASE, in green) of the dye at a concentration of 32 wt%. d) Schematic illustration of the relaxation processes and cavity losses that compete in the formation of a polariton BEC. The exciton reservoir is represented by the horizontal black line. From this energy an exciton can relax into a EP either by emission of a molecular vibration ($\Gamma_{\text{non-rad}}$, a non-radiative process that is linked to the Raman spectrum of the molecule) or by emission of a photon (Γ_{rad} , a radiative process that is linked to the photoluminescence spectrum). While the relaxation process increase the EP population, the finite lifetime τ_{LP} of the EP reduces it.

nanoparticles on top of a quartz substrate (fabrication details in Experimental Section), with a diameter and a height of 90 nm. A scanning electron microscope image of one of the arrays is shown in Figure 1b. Silicon is a semiconductor with a high refractive index and almost negligible absorption for wavelengths longer than 500 nm. Compared with noble metals commonly used in plasmonics, such as silver or gold, silicon has 100 times less absorption at 600–700 nm, which is the region of interest in our study (see Figure S1, Supporting Information). On top of the array, we deposit via spin-coating a layer with a thickness of 230 nm that consists of poly(methyl methacrylate) (PMMA) doped with the organic dye that will provide the excitons for the condensation. The coupling strength is proportional to \sqrt{N} , where N is the number of excitons within the mode volume of the optical resonance. Therefore, achieving strong coupling with organic molecules requires increasing their concentration within the polymer matrix of PMMA. We use a rylene dye [*N,N'*-bis(2,6-diisopropylphenyl)-1,7- and -1,6-bis(2,6-diisopropylphenoxy)-perylene-3,4:9,10-tetracarboximide], due to its high photostability and low aggregation at high concentrations. The absorption and photoluminescence (PL) of this dye embedded in PMMA at concentration of 32 weight percentage are shown in Figure 1c, and reveals several excitonic resonances. A concentration of 30–35 wt% is the limit that we can achieve with this dye. Higher concentrations result in aggregation of the molecules. The main absorption peak at 2.24 eV (553 nm) corresponds to the excitonic transition from the ground state to the first excited state. The second absorption peak at 2.41 eV (515 nm) is a vibrational replica of the excitonic transition, that is, a transition from the ground state to a vibronic sideband in the excited state. These peaks are also present in the PL of the dye. In addition, the amplified spontaneous emission is also shown in Figure 1c with the green curve.

Following a fast non-radiative relaxation after the optical pump, the exciton reservoir is formed at the lowest energy level of the excited states, which corresponds with the first excited state at 2.24 eV. This exciton reservoir is also known as the dark states (in a cavity with N emitters and 1 photon, there are 2 polaritonic states and $N-1$ states that are weakly coupled with the cavity and do not have a photonic component, and thus are referred as dark states). The excitonic resonance at 2.24 eV is the one that will be involved in the strong coupling and condensation of exciton-polaritons. Figure 1d illustrates schematically this excitonic reservoir (black-solid line) and the relaxation into the lower polariton (labeled as LP, represented by the red solid curve). Vibronic assisted relaxation is a non-radiative relaxation channel ($\Gamma_{\text{non-rad}}$), which depends on Raman active molecular vibrations.^[32–35] The Raman spectrum is displayed in the right panel of Figure 1d (blue curve) and shows that these vibrations are discrete and only a few allow an efficient transition from the reservoir to the LP states where condensation is possible (see the vertical blue arrow). On the other hand, radiative pumping (Γ_{rad}) is a relaxation channel that depends on the emission spectrum of the dye (orange filled curve in the right panel of Figure 1d).^[36–39] Competing with these relaxation channels is the polariton lifetime, illustrated in Figure 1d by the red wave-like arrows, which indicate the radiative decay of the exciton-polaritons.

Mie resonances in dielectric nanoparticles arise from the displacement currents inside the nanoparticle.^[40–42] However, these resonances still suffer from large radiative losses, which translates into broad resonances with low Q -factors. To circumvent this problem, arrays of nanoparticles are designed to support in-plane diffraction orders to which the Mie resonances can couple. In-plane diffraction orders, known as Rayleigh anomalies (RAs), arise when the periodicity of the array matches the wavelength of the incident light. RAs are pure photonic modes, with virtually no losses, that are delocalized over the periodic structure. As result, the coupling of RAs to Mie resonances results in hybrid Mie-RA resonances that are also delocalized and with low losses. These hybrid resonances are known as Mie surface lattice resonances or Mie-SLRs. SLRs have been already studied in great detail in plasmonic systems,^[43,44] and in recent years a number of works have investigated resonances in arrays of dielectric nanoparticle and Mie-SLRs.^[13,14,45] Thanks to the Mie character and the low losses, Mie-SLRs can produce large electromagnetic field enhancements, while they also inherit the dispersive character of the RAs (see Section S3, Supporting Information). Since the coupling strength between cavity and exciton increases with the dye concentration, the delocalization of the fields over the array is advantageous because it allows coupling with a large number of dye molecules. Therefore, it is not the Mie resonance of the individual particles which couples to the dye but the collective lattice resonance, the Mie-SLR, which we use here to achieve strong coupling. In fact the Mie resonance is at higher energies and it does not interact with the dye. Placing the Mie resonance at higher energy is not accidental and it allows to control the radiative losses. Radiative losses of Mie-SLRs can be easily controlled by the energy detuning between the Mie resonance and the RA, and Q -factors of 400–700 can be easily achieved with rational designs.^[14] This criteria dictates our choice of geometry. A silicon particle of 90 nm diameter and 90 nm height has a localized Mie resonance around 400 nm. To couple with the lowest excitonic transition, our cavity should be resonant around 580 nm. Since we want to study the overlap of the EP states with the vibronic transition and the PL of the dye, the cavity is negatively detuned with respect the exciton resonance. For this purpose, we choose the periods of $a = 400, 410,$ and 420 nm. The refractive index of PMMA ($n_{\text{PMMA}} = 1.49$) results in RAs from 600 to 630 nm ($\lambda_{\text{RA}} = n_{\text{PMMA}}a$). Another consequence of the size chosen for the silicon particles is that magnetic Mie resonances are not strongly supported. Indeed, since magnetic Mie resonances emerge as result of the circulation of the electric field inside the particle, a small diameter results in a weak magnetic mode.^[14] Consequently, the Mie-SLRs of these arrays have a dominant electric character.

The optical response of the cavity under broadband illumination is given in Figure 2 and shows the angle-resolved extinction for TM polarization and for the three samples (extinction = $1 - T/T_0$, where T is the transmission through the array and T_0 is the reference transmission). As it will be shown later, BEC occurs for the TM mode and, consequently, we focus on this polarization. Figure 2 is divided in three panels, each one for a different period of the Si nanoparticle array. The negative in-plane momenta k_{\parallel} in this figure corresponds to the extinction of the bare cavity formed by the Si nanoparticle array

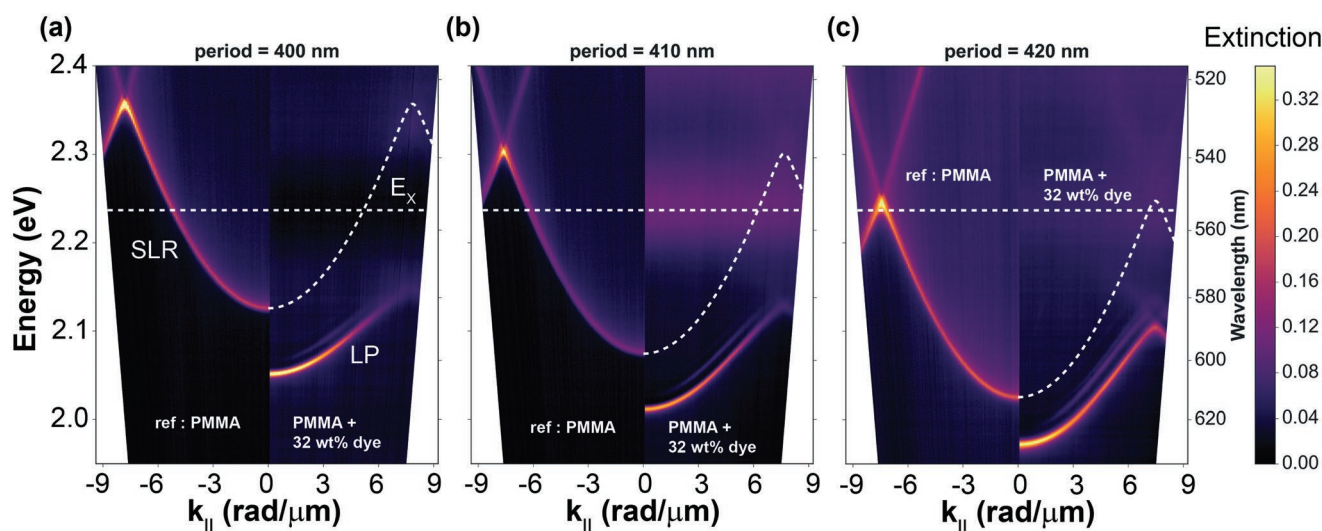


Figure 2. White light extinction measurements of the arrays under TM-polarized illumination. a–c) The measurements for the arrays with periods 400, 410, and 420 nm, respectively. The negative in-plane momenta k_{\parallel} represent the measurements performed on the bare cavity (undoped PMMA layer). The positive in-plane momenta k_{\parallel} represent the measurements performed on the cavity-dye system (PMMA + dye 32 wt%). The white horizontal lines represent the main exciton absorption peak of the dye, at energy E_x . The other white curves, only plotted for the cavity-dye system in the positive in-plane momenta space, represent the Mie-SLRs as fitted as the coupled oscillator model.

and a PMMA layer in the absence of the dye molecules. The measurements for the positive in-plane momenta correspond to the extinction of the coupled system formed by the Si nanoparticle array and the PMMA layer doped with dye. The in-plane momentum is defined as $k_{\parallel} = 2\pi n/\lambda \sin \theta_{\text{in}}$ where λ is the wavelength of light, and θ_{in} is the incident angle of the light with respect to the sample normal. The RAs are calculated with the grating equation (see Section S3, Supporting Information). For the incident TM polarization, the coupling of the Mie resonance is with the $(0, \pm 1)$ RAs. Figure S3, Supporting Information, shows that $(1, \pm 1)$ RAs are also present and are in fact observed in the measured extinction. The $(1, \pm 1)$ RAs are responsible of the down-bending of the Mie-SLR at large k_{\parallel} .

In presence of the dye in high concentration, the Mie-SLRs strongly couple with the excitons and two new eigenstates emerges: the upper and lower exciton-polaritons (UP and LP, respectively). The LP is clearly visible in the measured wavelength range, where a pronounced shift relative to the bare cavity mode due to the coupling is apparent. A clear signature of strong coupling is the anti-crossing behavior of the new eigenstates, which can be noticed for the LP at large k_{\parallel} for the three arrays. Due to the different periodicities, the Mie-SLRs of each array have a different detuning from the exciton resonance, which we measure as -102 , -153 , and -204 meV for the periods of 400, 410, and 420 nm, respectively. Mie-SLRs are characterized by a very narrow linewidth over the whole range of k_{\parallel} , and this is inherited as well by the LP, with values of 5–6 meV at $k_{\parallel} = 0$, which are measured as a half-width at half-maximum using a single peak fitting. The inverse of this line width is proportional to the resonance life time and this is translated into 50–70 fs approximately. Another aspect inherited by the LP is the electric character of the Mie-SLR.^[30] In addition to the LP, we observe a weaker dispersive mode that becomes dark close to normal incidence. Calculations, given in Section S4, Supporting Information, show that this mode

corresponds with an out-of-plane electric dipole Mie-SLR which has vanishing extinction at $k_{\parallel} = 0$. We obtain the Rabi energy of each array using two coupled-oscillator models (see the Experimental Section), one used to fit the Mie-SLR (coupling between the electric dipole Mie resonance and the RAs), and the other used to fit the LP (coupling between Mie-SLRs and excitons). From the fit of the LP we find the following values of the Rabi energy: $\hbar\Omega \approx 300$ meV for the three arrays. The fit to the Mie-SLR is plotted with white-dashed curves. The horizontal white dashed line represents the energy of the excitons.

2.2. Condensation and Non-Linear Emission

To investigate the condensation of EPs in arrays of Si nanoparticles, we excite them non-resonantly with 100 fs and 1 kHz repetition rate pulses at $\lambda = 400$ nm and measure the angle-resolved photoluminescence spectra as a function of the incident excitation power. To avoid long exposures of the sample with the pump, which can damage the array and photobleach the dye, we measure the angle-resolved spectra using a back-focal plane imaging technique (details in Experimental Section). A polarizer allows us to distinguish between TE and TM polarized emission. Below threshold, the PL spectrum of the three arrays is dominated by the spontaneous decay of the LP (see Figure 3a–c for the periods of 400, 410, and 420 nm, respectively). The PL below threshold is maximum at the bottom of the LP, close to $k_{\parallel} = 0$, indicating efficient relaxation by radiative pumping.^[37]

When the excitation fluence is increased beyond a certain threshold, the emission collapses at the bottom of the LP. Remarkably, this collapse is observed for the three arrays. The angle-resolved emission at an excitation fluence slightly above threshold is shown in Figure 3d–f for the periods of 400, 410, and 420 nm, respectively. The collapse in the emission is

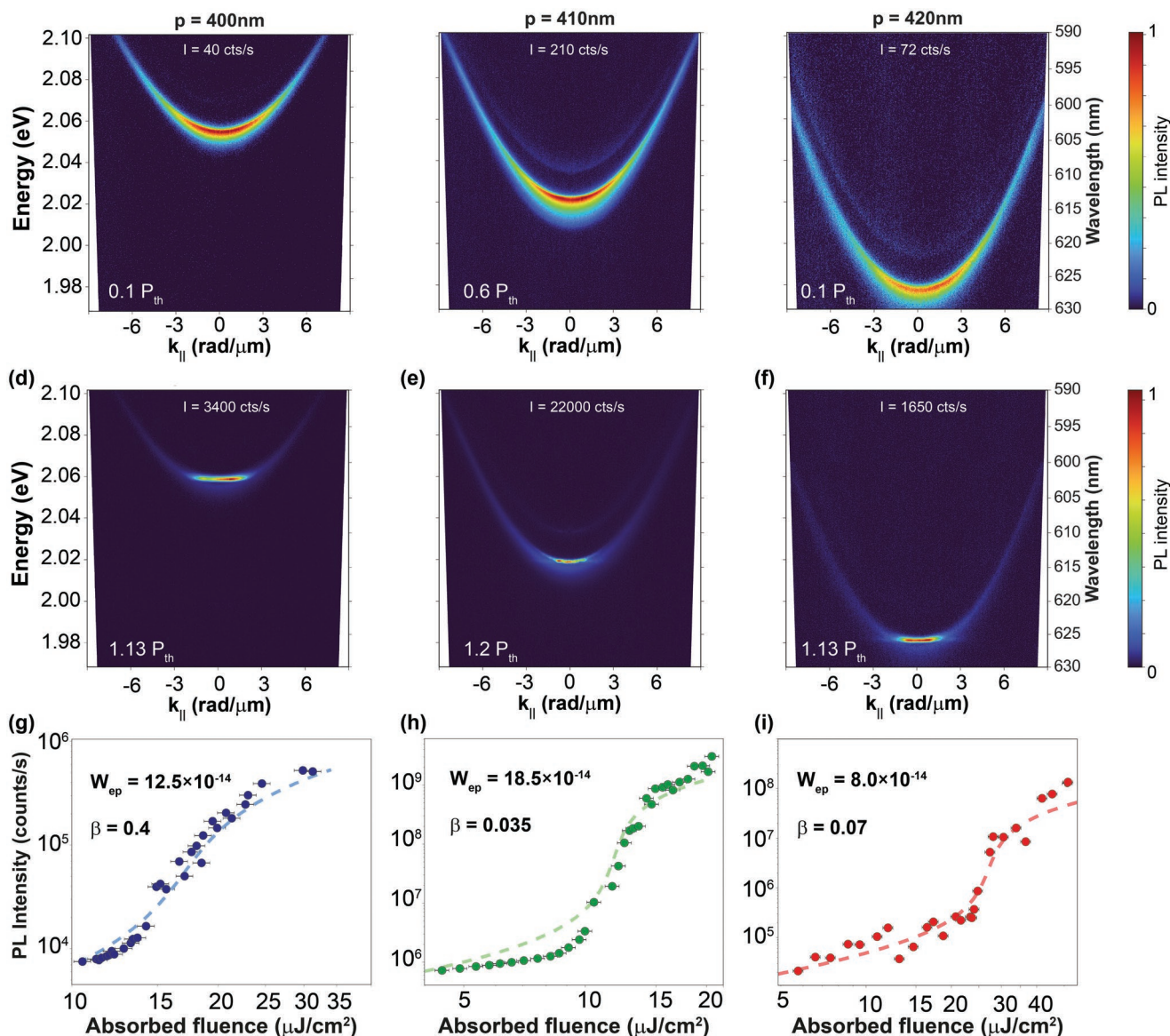


Figure 3. Angle-resolved photoluminescence of the arrays with 32 wt% dye concentration below threshold (a–c), and above threshold (d–f). Panels (a,d), (b,e), and (c,f) represent the measurements for the arrays with periods of 400, 410, and 420 nm, respectively. The emission intensities in unit of counts s^{-1} of the brightest pixel are indicated for each array in each panel, together with the pump fluences in units of the threshold pump. g–i) Integrated emission intensity in counts s^{-1} at $k_{\parallel} = 0$ as function of the absorbed pump fluence for the arrays with periods of 400, 410, and 420 nm, respectively. The experimental data is shown as circles. In addition, we show the result of the fit with the master equation (see Equations (1) and (2)), in the dashed line for each panel. The fitting is obtained for values of W_{ep} and β , which are shown in each panel.

observed at $k_{\parallel} = 0$ as the emergence of a narrow peak, which dominates the spectrum upon increasing the pump power (see Figure S6, Supporting Information). Following the threshold, we observe a non-linear increase in the emission intensity close to $k_{\parallel} = 0$ for the three arrays, which are shown in Figure 3g–i. From these last three figures we obtain the thresholds 13.5, 8.2, and 21.6 $\mu J cm^{-2}$ for the periods of 400, 410, and 420 nm, respectively.

We describe next the characterization of the signatures of the BEC: spatial and temporal coherence, polarization of the emission, and blue shift of the condensation energy with pump fluence. The temporal coherence is related to the linewidth of

the emission. **Figure 4a** shows a narrowing in the linewidth upon achieving the condensation threshold, which implies an increase in temporal coherence. The reduced losses of the dielectric metasurface are evident in the narrow line widths close to 1 meV. To observe the spatial coherence, we have measured the field amplitude auto-correlation of the BEC emission using a Michelson interferometer. The emission from the condensate is split in two beams. One of the beams remains unaltered, while the other is sent to a retro-reflector where the image is inverted. Another mirror brings the two images together and we use a camera to record their interference. These results are displayed in Section S6, Supporting Information. The emission

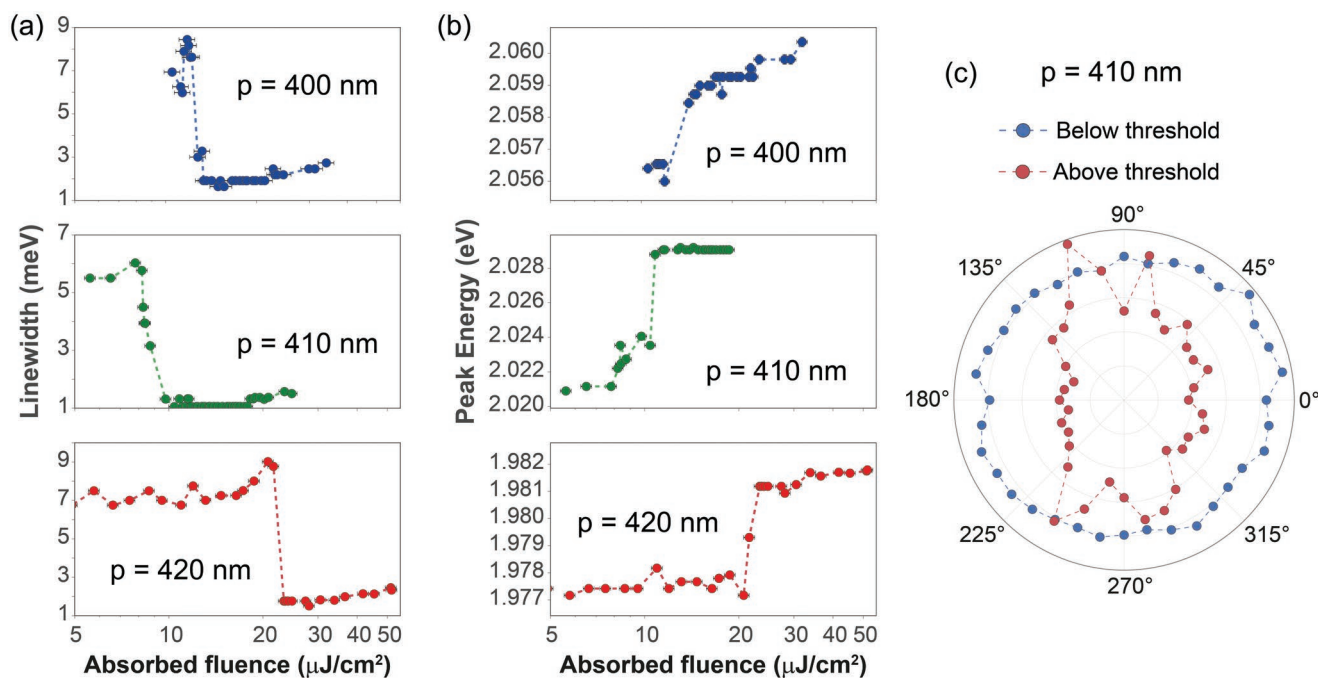


Figure 4. a) Linewidth of the emission peak at $k_{\parallel} = 0$ as function of the absorbed pump fluence for the three arrays. b) Peak energy of the emission at $k_{\parallel} = 0$ as function of the absorbed pump fluence for the three arrays. c) Polarization of the emission below (blue dots) and above (red dots) threshold for the array with period of 410 nm.

does not show any interference below threshold, indicating incoherent spontaneous emission. Furthermore, the shape of the emission below threshold is given by the shape of the pump beam. However, we observe interference in the emission above threshold. This interference is particularly clear for the arrays with period 400 and 410 nm, indicating the extended spatial coherence of the condensate.

Another characteristic of a polariton BEC is the buildup of polarization, due to the collapse of the EP population to the ground state of the LP. We rotate the polarizer in our setup and record the emission at $k_{\parallel} = 0$ as function of the polarization angle. Figure 4b shows that below threshold the emission is unpolarized (blue circles), which is explained by the symmetry of the array at $k_{\parallel} = 0$. In a square array, the symmetry imposes the indistinguishability between the RAs at $k_{\parallel} = 0$, that is, the $(0, \pm 1)$ and the $(\pm 1, 0)/(-1, 0)$ RAs are degenerate. As a result, the LP has the same energy at $k_{\parallel} = 0$ for any incident polarization. By reciprocity, the same holds in the emission and, consequently, this emission is unpolarized. However, the TM mode is responsible of the condensation above threshold, and the measurements of the polarization in the emission confirm it (see red dots in Figure 4b).

The blue shift of the emission peak with the pump fluence that can be appreciated in Figure 4c is another important characteristic of BECs. This blue shift is well understood for inorganic semiconductors and is explained as the result of repulsive Coulomb exchange-interactions between the Wannier–Mott exciton-polaritons. However, this blue shift is still a subject of debate for organic materials, where the localized nature of Frenkel excitons decreases the strength of Coulomb interactions.^[46,47]

2.3. Tunable Energy of the Condensation Enabled by Radiative Pumping

The decrease in material losses also reduces the absorption of light emitted by the excitons in their radiative decay, and allows for another relaxation mechanism that contributes to the buildup of the polariton population: radiative pumping. This mechanism was proposed theoretically more than a decade ago, but it was only in the last years that its relevance was experimentally demonstrated.^[32,36,37,39,48–50] Early works in organic BECs attributed the buildup of the EP population to the vibronic assisted scattering (VAS) of the uncoupled excitons in the reservoir (i.e., the dark states), which is a non-radiative process.^[5,7,33,34] VAS relies thus in the vibrational spectrum of organic molecules. Excitons are coupled to these vibrations, which means that an exciton can emit a vibrational quanta and relax to a lower energy state. However, these vibrations have a well-defined energy and do not form a continuous spectrum. Consequently, VAS becomes only efficient for BEC if the transition of the reservoir excitons is close to the lowest energy state of the LP at $k_{\parallel} = 0$, where the condensate is formed. The condensation energy is thus defined by the internal structure of the molecules when VAS dominates the relaxation.

On the other hand, the emission of the dye is broad in energy, which allows a buildup of EP population at $k_{\parallel} = 0$ as long as the polariton states overlap with the emission spectrum of the dye.^[36] This characteristic explains why we observe BEC at different energies for the different arrays even though the same dye is used for the three samples. We note that a similar result has been recently reported by Ishii et al.^[50] Radiative pumping is probably also responsible of the broadband polariton lasing

observed in the work by Sannikov et al.^[51] However, the exact mechanisms of the radiative pumping of EPs are not yet well understood. It is believed that the radiative pumping involves the vibronic replica in the emission spectrum, but there is no experimental evidence of this yet.^[36] More importantly, the role of optical absorption in the cavity on the radiative pumping has not been investigated so far. The work of Ramezani et al. with arrays of plasmonic nanoparticles showed condensation at the same energy for arrays with different periods.^[9] These results strongly suggest that the radiative pumping mechanism is suppressed in the plasmonic systems due to the large Ohmic losses and the concomitant absorption in the metal. Therefore, metals will not only reduce the lifetime of the EP, but they will also reduce the efficiency of the radiative pumping toward BEC.

2.4. Threshold Dependence on the Array Period

The threshold for BEC depends on the efficiency of the EP buildup in the LP at $k_{\parallel} = 0$. This efficiency is given, among other factors, by the energy overlap of the vibrational and photoluminescence spectra with the LP at $k_{\parallel} = 0$. The value of this overlap determines the relaxation rate of the excitons in the reservoir into the LP. In our experiments, the energy of the LP at $k_{\parallel} = 0$ changes with the period of the array, which affects the overlap with the vibrational and emission of the dye and explains the different thresholds observed in Figure 3g–i. To understand this dependence better, we have measured as well the condensation thresholds using a layer of identical thickness but with a lower concentration of dye of 22 wt%. Measurements of the optical extinction and the emission above threshold are given in Section S7, Supporting Information. **Figure 5a** shows the values of the thresholds for high (32 wt%, red dots) and low (22 wt%, blue dots) dye concentrations, respectively. The lower concentration leads to a general increase in the condensation threshold when compared with the thresholds at high concentration. The array with period 410 nm is for both concentrations the sample

with lowest threshold. For periods different than 410 nm, the threshold increases. However, the trend of this increase is very different for high and low dye concentrations: first, the sample with a period of 420 nm has the highest threshold at high concentrations, but the highest threshold occurs for the period of 400 nm at low concentrations. Second, the sample with a period of 420 nm experiences the smallest increase in threshold when reducing the dye concentration, while the sample with a period of 400 nm experiences the largest increase.

To gain insight in the relationship between the condensation threshold and the relaxation rate of the excitons in the reservoir, we use a kinetic model to quantitatively describe the population dynamics of the EPs and the exciton reservoir and to extract W_{ep} ^[36,50]

$$\frac{dn_R}{dt} = \left(1 - \frac{n_R}{N_0}\right)P(t) - \frac{n_R}{\tau_R} - k_b n_R^2 - W_{ep} n_R n_{LP}, \quad (1)$$

$$\frac{dn_{LP}}{dt} = W_{ep} n_R n_{LP} + \beta \frac{n_R}{\tau_R} - \frac{n_{LP}}{\tau_{LP}}, \quad (2)$$

where n_R and n_{LP} are the density of excitons in the reservoir and of EPs at the condensation energy, respectively. The exciton population decays through spontaneous emission with a lifetime τ_R and exciton–exciton annihilation with a rate k_b , while the EPs decay radiatively with a lifetime τ_{LP} . A fraction β of the excitons that decay through spontaneous emission populates the LP. We consider the generation of reservoir excitons in Equation (1) through a pulsed laser, that is the pump, which we model as a Gaussian temporal pulse of 150 fs full-width at half-maximum (FWHM). The term N_0 represents the molecular density and is introduced to account for saturation effects. This kinetic model is similar to the master equation for a photon laser,^[52] but with the difference that the relaxation rate W_{ep} involves a transition between the exciton reservoir and the LP that does not require population inversion.

With this model, we can calculate the emission intensity by the integral of the EP population for each pump fluence as

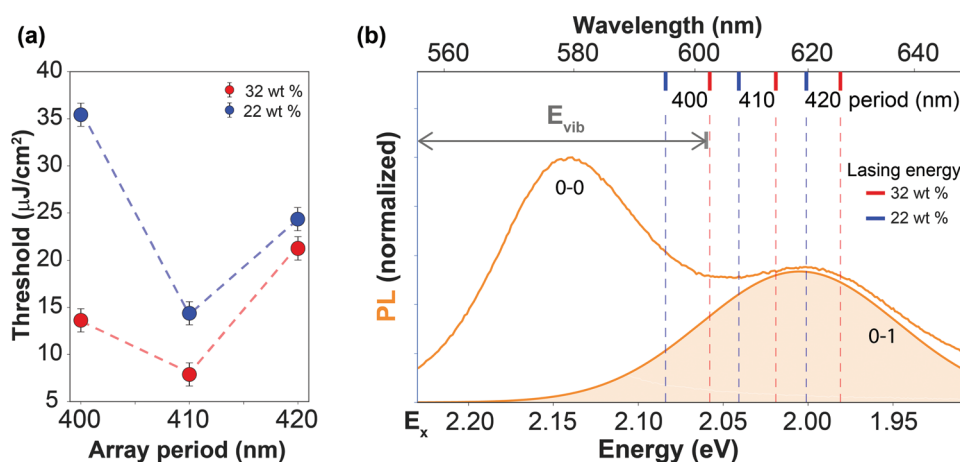


Figure 5. a) Condensation threshold for the three arrays studied at high concentration (red dots and red dashed line) and low concentration (blue dots and blue dashed line). b) Condensation energies of the three arrays at high (red dashed lines) and low (blue dashed lines) concentrations. The orange curve represents the emission of the dye, while the orange area is a Gaussian fit of the vibronic replica in the emission, labeled as (0–1). The energy axis starts at the energy the exciton reservoir, which corresponds with the main absorption peak E_x (see Figure 1d). The known vibrational relaxation E_{vib} is represented by the grey arrow.

Table 1. Experimental threshold P_{th} (in red) and calculated relaxation rate W_{ep} (in blue) using Equations (1) and (2) for the concentrations of dye at 32 wt% and at 22 wt%.

Period [nm]	400	410	420
32 wt% : P_{th} [$\mu\text{ cm}^{-2}$]	13.5	8.1	21.6
32 wt% : W_{ep} [$10^{-14}\text{ cm}^3\text{ s}^{-1}$]	12.5	18.5	8
22 wt% : P_{th} [$\mu\text{ cm}^{-2}$]	35.7	14.3	24.3
22 wt% : W_{ep} [$10^{-14}\text{ cm}^3\text{ s}^{-1}$]	2.5	9.5	2.8

$I \propto \int_0^{\infty} n_{LP}(t) dt$. The results of the fits to the measurements are

shown in Figure 3h,i and the parameters of the fits are given in Table 1. The factor β and the relaxation rate W_{ep} are treated as free fitting parameters. Given that the lifetime of the dye and of the polariton is similar across the different arrays, it is the relaxation rate W_{ep} which influences the value of the condensation threshold. The fits confirm this and indeed the lowest threshold for the array with period 410 nm corresponds with the largest relaxation rate.

With the aim of understanding the different physical mechanisms leading to condensation, we plot in Figure 5b the emission (orange curve), together with the condensation energies of the arrays (vertical red lines correspond to 32 wt%, and blue lines to 22 wt%). The axis of the energy starts in the left at the value of $E_X = 2.23$ eV. We also indicate in this figure the energy of the vibrational relaxation known to assist condensation in this dye, $E_{vib} \approx 170$ meV, and its position in the spectrum at $E_X - E_{vib} = 2.06$ eV. The gray arrow in Figure 5b represents the vibrational relaxation from the reservoir toward $E_X - E_{vib}$. Ultrafast dynamics of the polariton condensation in arrays of plasmonic nanoparticles with this dye did not reveal other molecular vibrations playing a role in the VAS.^[53]

Currently, the details of radiative pumping are not fully understood. The most comprehensive model to date, derived by Mazza et al. describe radiative pumping as a vibronic progression, and therefore it only involves the vibronic replica of the photoluminescence.^[36] We have plotted the vibronic replica, obtained as a Gaussian fit to the emission spectrum, in Figure 5 as the orange area and labeled it as (0–1). In context of the theory by Mazza et al., we observe that the array with period of 410 nm at 32 wt% has the largest overlap of the three arrays with the (0–1) emission. On the other hand, the array with period of 400 nm overlaps with the vibronic progression. This differences in overlap could explain the lowest condensation threshold for the array of 410 nm and why the array with period of 400 nm has a lower threshold than the array with period of 420 nm. Reducing the dye concentration decreases the value of the Rabi splitting and therefore blueshifts the position of the LP at $k_{||} = 0$, changing the overlaps with the (0–1) emission and the vibrational mode. In this case we find that the array with period of 400 nm now has the highest condensation threshold. Looking at the condensation energy of the array with period of 400 nm in Figure 5, we can see that now the overlap with the vibration and the (0–1) emission is very low. Interestingly, the array with period of 410 nm still results in the lowest threshold, although the array with period of 420 nm has now a better overlap with the (0–1) emission. These results clearly

show that in addition to the radiative pumping described by Mazza et al.,^[36] VAS plays an important role in the relaxation toward EP condensation when there is an overlap with a vibrational model. Understanding both VAS and radiative pumping better is therefore critical to achieve the largest possible relaxation rate that an organic molecule can offer in a cavity. Recent efforts in understanding better the radiative pumping by Grant et al., have suggested that the quantum yield of the organic emitter directly impacts the rate of the radiative pumping,^[37] and Groenhof et al., describes that whether radiative pumping or VAS are dominant is influence by the Stokes shift of the organic emitter.^[38]

2.5. Discussion: Lowering the Condensation Threshold through Engineering of the Radiative Losses

The system of Equations (1) and (2) show that the condensation threshold depends on the relaxation rate W_{ep} and the lifetime of the EPs and the exciton reservoir, τ_{LP} and τ_R , respectively. The lifetime of the exciton in the cavity is largely unaffected by the cavity due to its large mode volume. The impact of this value is connected with the emission quantum efficiency of the dye and, as mentioned by Grant et al., it is important for radiative pumping that the dye has a high quantum efficiency.^[37] Leaving aside the properties of the dye, it is important to pay attention to the role of the cavity losses, which determines τ_{LP} . As we have seen, the use of dielectric metasurfaces reduces the losses in the EP states, allowing for the radiative pumping and the increase of the relaxation rate. Lower losses and increased relaxation rates are responsible of the observed low thresholds. However, we note that even in our metasurface, the remaining radiative losses still compete with the relaxation rate. The quality factor of the LP mode at $k_{||} = 0$ is in the order of 400, which gives a polariton lifetime of 50–60 fs. Since the main source of loss is radiative outcoupling, there is still room to reduce the condensation threshold by increasing the lifetime of the cavity modes involved in the strong coupling. Therefore, there is still room to reduce the condensation threshold by reducing even further the radiative losses. To determine how large can be the reduction in threshold, we use again the kinetic model given by Equations (1) and (2). We assume the relaxation rate of the array with period of 410 nm at a high dye concentration and we calculate the fluence-dependent integrated emission as function of the EP lifetime, τ_{LP} . The results of the calculations are displayed in Figure 6. The color in this figure indicates the intensity of the emission. Below threshold, the emission grows almost linearly and is after the threshold that the emission grows non-linearly. For a line with function $f(x)$, the second derivative with respect to x is zero. Therefore we calculate the threshold as the point where the second derivative becomes non-zero, that is, $P_{th} = P[\frac{\partial^2 \log_{10}(I)}{\partial P^2} > 0]$. Figure 6 shows a non-linear decrease in the threshold as function of the EP lifetime. At short EP lifetimes, the cavity loss rate exceeds the relaxation rate and the threshold diverges as the EP lifetime approaches zero. At long lifetimes, $\tau_{LP} > 500$ fs, the threshold reaches the lowest values, and further increasing the lifetimes does not bring any significant reduction of this threshold.

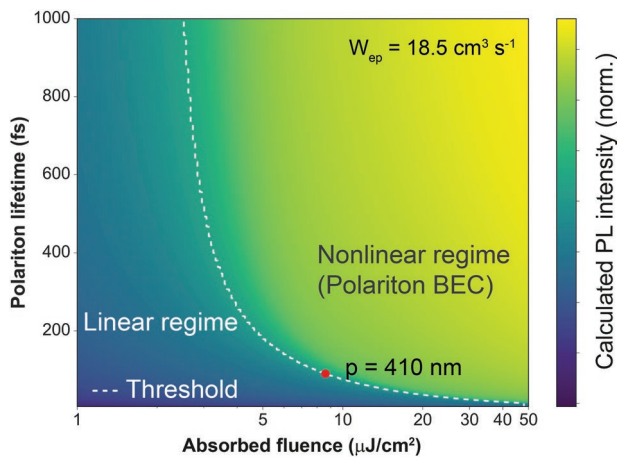


Figure 6. Calculated emission intensity of a polariton population as function of absorbed pump fluence and polariton lifetime. The color scale determines the intensity of the emission. The results are obtained using the master equation and the relaxation rate obtained from fitting the array with period of 410 nm at the high concentration of dye. The white dashed line defines the threshold of the condensation. To the left side of the threshold, there is no condensation, and the polariton emission is in the linear regime. The red dot represents the threshold observed for the array with period of 410 nm.

These results provide two important conclusions: the first one is that, even with long cavity lifetimes, there is a limit in the condensation threshold set by the exciton relaxation rate into the LP. By exploiting better the vibrational relaxation and radiative pumping of organic dyes, it should be possible to improve the relaxation rates. Second, the reduction in the threshold is most significant for the first few 100 fs of the EP lifetime. This lifetime is dominated by the cavity lifetime. Achieving cavity lifetimes longer than 100 fs with microcavities is challenging, requiring complex hemispherical cavities. However, dielectric metasurfaces offer a promising alternative, through the so-called bound states in the continuum (BICs). Indeed, conventional photon lasing in BIC metasurfaces has been already demonstrated and is becoming an increasing topic of research.^[23,27,28,54] Thanks to the suppression of radiative losses, the lifetime of the cavity becomes infinite in a BIC mode if there is no material absorption.^[15] Just a few works have explored the possibilities that BIC resonances could bring to strong light–matter coupling and in particular to polariton lasing.^[55,56] Very recently, condensation from a BIC mode has been demonstrated in a sub-wavelength grating etched on top of a multi quantum well GaAs heterostructure.^[57]

3. Conclusion

We have demonstrated the first condensate based on an open all-dielectric metasurface using organic emitters. By exploiting the low material losses of silicon in the visible and by making use of the diffractive coupling between the Mie resonances in the nanoparticles forming the array, we are able to significantly reduce the radiative losses as well. This behavior is inherited in the EPs, which show remarkably narrow linewidths. As a consequence, we observe the threshold for non-equilibrium

condensation at very low excitation fluences of a few $\mu\text{J cm}^{-2}$. The impact of losses in the condensation of EPs has not been discussed in detail in the existing literature. Here, we show that the losses are critical for the threshold, but also that the radiative relaxation of the excitons into the polariton states play a very important role in the definition of the condensation threshold. Our work shows the potential impact that all-dielectric metasurfaces could bring to the field of BECs of exciton-polaritons. By tailoring bound states in the continuum and optimizing the relaxation rate of the dye, we believe it is possible to achieve thresholds below $\mu\text{J cm}^{-2}$.

4. Experimental Section

Fabrication: Polycrystalline Si thin films with a thickness of 90 nm were grown on a synthetic silica glass substrate by low-pressure chemical vapor deposition using SiH_4 gas as a source of Si. A resist (NEB22A2, Sumitomo) was cast on the Si film and exposed to electron-beam lithography, followed by development to make nanoparticle arrays of resist on the Si film. The Si film was vertically etched using a selective dry etching (Bosch process) with SF_6 and C_4F_8 gases, and the resist residue was etched away by oxygen dry etching. The fabricated area of the array covered $5 \times 5 \text{ mm}^2$.

Experimental Characterization: To measure the angle-resolved dispersion under white light illumination, the sample was placed in a rotational stage and illuminated by a collimated and polarized beam from an halogen lamp. The angle of incidence of the illumination was controlled with the rotational stage. The area of illumination had a diameter of 1 mm. The detector was fixed along the optical beam, so the zeroth-order transmission was measured. The incident in-plane momentum and angle of incidence were related to each other with the expression $k_{\parallel} = \frac{2\pi n}{\lambda_0} \sin\theta_i$, where λ_0 is the free-space wavelength and n is refractive index of the glass. The extinction was calculated as $E = 1 - T_0/T_{0, \text{ref}}$, where T_0 and $T_{0, \text{ref}}$ are the zeroth-order transmission measured on and off the array. The spectra was measured with a fiber-coupled spectrometer (USB 2000, Ocean Optics) with 0.3 nm spectral resolution.

A Fourier imaging setup was used to measure the angle-resolved emission. The pump pulses were generated with a Ti:sapphire regenerative amplifier (Coherent Astrella), having a wavelength of 800 nm, a duration of 150 fs and a repetition rate of 5 kHz. The pulses are frequency doubled to 400 nm before being sent into the setup to pump the sample non-resonantly. To avoid damage in the sample, the rate was decreased to 1 kHz with a mechanical chopper. The pump was focused by a lens on the sample and the emission was collected with a microscope objective (Nikon CFI S Plan Fluor ELWD 40XC, with a numerical aperture of 0.6). The excitation spot had an approximate diameter of 800 μm . A long-pass filter for $\lambda = 500 \text{ nm}$ and a linear polarizer were placed after the objective to block the pump and select the polarization of the emission. The emission was sent into an imaging spectrometer Princeton Instruments Acton Series 2300 with a CCD camera ProEM 512B.

Coupled-Oscillator Model for the Mie-SLR: The Mie-SLRs were fitted with a coupled oscillator model that defined the coupling between the Mie resonances in the nanoparticles and the RAs supported by the array. Each polarization had different RAs because the Mie resonances couple preferentially along a given direction, namely, the direction perpendicular to the orientation of the dipole moment. The main interest was in the TM polarization, which gave the following matrix to diagonalize for each value of the incident in-plane momentum k_{\parallel} :

$$\mathbf{A}_{\text{Mie-SLR}}(k_{\parallel}) = \begin{pmatrix} \tilde{E}_{\text{Mie}} & \mathbf{g}_{\text{Mie}-(0,\pm 1)\text{RA}} & \mathbf{g}_{\text{Mie}-(-1,\pm 1)\text{RA}} \\ \mathbf{g}_{\text{Mie}-(0,\pm 1)\text{RA}} & \tilde{E}_{\text{RA-TM}(0,\pm 1)} & \mathbf{g}_{\text{RA-RA}} \\ \mathbf{g}_{\text{Mie}-(-1,\pm 1)\text{RA}} & \mathbf{g}_{\text{RA-RA}} & \tilde{E}_{\text{RA-TM}(-1,\pm 1)} \end{pmatrix}, \quad (3)$$

where \tilde{E} refers to the complex energy, $\tilde{E} = E + i\gamma/2$, with E the resonance energy and γ the linewidth. \tilde{E}_{Mie} , $\tilde{E}_{\text{RA-TM}}(0, \pm 1)$, and $\tilde{E}_{\text{RA}}(-1, \pm 1)$ refers to the Mie resonance, the $(0, \pm 1)$ RA, and the $(-1, \pm 1)$ RA, respectively. The energy and linewidth of the Mie resonance were set as $E_{\text{Mie}} = 3.025$ eV and $\gamma_{\text{Mie}} = 0.15$ eV. The coupling strength with the two RAs, $g_{\text{Mie}-(0, \pm 1)\text{RA}}$ and $g_{\text{Mie}-(1, \pm 1)\text{RA}}$, were the free parameter for fitting of the measured Mie-SLR. Two RAs were used because both were present under TM illumination in a square lattice at energies that allow hybridization with the Mie resonance. Since the RAs were purely photonic modes, they do not interact with each other, making $g_{\text{RA-RA}} = 0$. Ideally, there will be no losses for the RAs, but there is always some scattering due to fabrication imperfections and γ_{RA} was set as 0.001 eV. Figure S3, Supporting Information, in the SM plots these diffraction orders and the associated Mie-SLRs, which accurately matched the measured Mie-SLRs.

Coupled-Oscillator Model for the Exciton-Polariton: The new eigenstates were fit in the strong coupling regime using a coupled oscillator model that described the interaction between the Mie-SLRs obtained from Equation (3) and the excitons as function of the incident in-plane momentum k_{\parallel}

$$\mathbf{A}_{\text{light-matter}}(k_{\parallel}) = \begin{pmatrix} \tilde{E}_{\text{M-SLR}}(k_{\parallel}) & \hbar\Omega/2 \\ \hbar\Omega/2 & \tilde{E}_{X_1} \end{pmatrix} \quad (4)$$

where $\tilde{E}_{\text{M-SLR}}(k_{\parallel})$ is the complex energy obtained from the diagonalization of Equation (3), except for the losses, $\gamma_{\text{M-SLR}}$, which was obtained from the measurements. Similarly, E_{X_1} is the exciton resonance corresponding to the exciton transition energy $E_{X_1} = 2.237$ eV and a linewidth of 0.03 eV. The Mie-SLR for TM polarization does not couple with the vibronic replica that was observed in the absorption spectrum in Figure 1d at 2.42 eV and it was not included in the model. The coupling strength, which is the fitting parameter, is $g = \hbar\Omega/2$ where Ω is the Rabi frequency.

Supporting Information

Supporting Information is available from the Wiley Online Library or from the author.

Acknowledgements

This work was financially supported by the Dutch Organization for Scientific Research (NWO) through the Gravitation grant "Research Centre for Integrated Nanophotonics" and through the Innovational Research Activities Scheme (Vici project no. 680-47-628). The authors also gratefully acknowledge financial support from the Ministry of Education, Culture, Sports, Science and Technology (MEXT), Japan (22H01776), JSPS collaborative work (JPJSBP120219920), and the Asahi Glass Foundation. The authors sincerely thank Jose Sanchez Gil, Diego Romero Abujetas, and Alvaro Buendia for the insights in CEMD, the use of their CEMD code to understand the cavity modes of the samples, and the discussions and calculations about the vibrational relaxation of reservoir excitons.

Conflict of Interest

The authors declare no conflict of interest.

Data Availability Statement

The data that support the findings of this study are available from the corresponding author upon reasonable request.

Keywords

all-dielectric metasurfaces, Bose–Einstein condensation, coherent emission, exciton-polaritons

Received: September 30, 2022

Revised: December 10, 2022

Published online: January 25, 2023

- [1] H. Deng, H. Haug, Y. Yamamoto, *Rev. Mod. Phys.* **2010**, *82*, 1489.
- [2] A. Imamog, R. Ram, S. Pau, Y. Yamamoto, *Phys. Rev. A* **1996**, *53*, 4250.
- [3] A. Amo, J. Lefrère, S. Pigeon, C. Adrados, C. Ciuti, I. Carusotto, R. Houdré, E. Giacobino, A. Bramati, *Nat. Phys.* **2009**, *5*, 805.
- [4] J. Kasprzak, M. Richard, S. Kundermann, A. Baas, P. Jeambrun, J. M. J. Keeling, F. Marchetti, M. Szymańska, R. André, J. Staehli, V. Savona, P. B. Littlewood, B. Deveaud, L. S. Dang, *Nature* **2006**, *443*, 409.
- [5] S. Kéna-Cohen, S. Forrest, *Nat. Photonics* **2010**, *4*, 371.
- [6] T. Boulier, M. J. Jacquet, A. Maître, G. Lerario, F. Claude, S. Pigeon, Q. Glorieux, A. Amo, J. Bloch, A. Bramati, E. Giacobino, *Adv. Quantum Technol.* **2020**, *3*, 2000052.
- [7] J. D. Plumhof, T. Stöferle, L. Mai, U. Scherf, R. F. Mahrt, *Nat. Mater.* **2014**, *13*, 247.
- [8] T. Cookson, K. Georgiou, A. Zasedatelev, R. T. Grant, T. Virgili, M. Cavazzini, F. Galeotti, C. Clark, N. G. Berloff, D. G. Lidzey, P. G. Lagoudakis, *Adv. Opt. Mater.* **2017**, *5*, 1700203.
- [9] M. Ramezani, A. Halpin, A. I. Fernández-Domínguez, J. Feist, S. R.-K. Rodriguez, F. J. Garcia-Vidal, J. G. Rivas, *Optica* **2017**, *4*, 31.
- [10] A. I. Väkeväinen, A. J. Moilanen, M. Nečada, T. K. Hakala, K. S. Daskalakis, P. Törmä, *Nat. Commun.* **2020**, *11*, 3139.
- [11] P. R. Dolan, G. M. Hughes, F. Grazioso, B. R. Patton, J. M. Smith, *Opt. Lett.* **2010**, *35*, 3556.
- [12] B. Wang, P. Yu, W. Wang, X. Zhang, H.-C. Kuo, H. Xu, Z. M. Wang, *Adv. Opt. Mater.* **2021**, *9*, 2001520.
- [13] A. B. Evlyukhin, C. Reinhardt, A. Seidel, B. S. Luk'yanchuk, B. N. Chichkov, *Phys. Rev. B* **2010**, *82*, 045404.
- [14] G. W. Castellanos, P. Bai, J. Gómez Rivas, *J. Appl. Phys.* **2019**, *125*, 213105.
- [15] C. W. Hsu, B. Zhen, A. D. Stone, J. D. Joannopoulos, M. Soljačić, *Nat. Rev. Mater.* **2016**, *1*, 16048.
- [16] D. Marinica, A. Borisov, S. Shabanov, *Phys. Rev. Lett.* **2008**, *100*, 183902.
- [17] K. Koshelev, S. Lepeshov, M. Liu, A. Bogdanov, Y. Kivshar, *Phys. Rev. Lett.* **2018**, *121*, 193903.
- [18] S. Liu, A. Vaskin, S. Addamane, B. Leung, M.-C. Tsai, Y. Yang, P. P. Vabishchevich, G. A. Keeler, G. Wang, X. He, Y. Kim, N. F. Hartmann, H. Htoon, S. K. Doorn, M. Zilk, T. Pertsch, G. Balakrishnan, M. B. Sinclair, I. Staude, I. Brener, *Nano Lett.* **2018**, *18*, 6906.
- [19] A. Vaskin, S. Mashhadi, M. Steinert, K. E. Chong, D. Keene, S. Nanz, A. Abass, E. Rusak, D.-Y. Choi, I. Fernandez-Corbaton, T. Pertsch, C. Rockstuhl, M. A. Noginov, Y. S. Kivshar, D. N. Neshev, N. Noginova, I. Staude, *Nano Lett.* **2019**, *19*, 1015.
- [20] T. Bucher, A. Vaskin, R. Mupparapu, F. J. Löchner, A. George, K. E. Chong, S. Fasold, C. Neumann, D.-Y. Choi, F. Eilenberger, F. Setzpfandt, Y. S. Kivshar, T. Pertsch, A. Turchanin, I. Staude, *ACS Photonics* **2019**, *6*, 1002.
- [21] I. Staude, T. Pertsch, Y. S. Kivshar, *ACS Photonics* **2019**, *6*, 802.
- [22] E. Khaidarov, Z. Liu, R. Paniagua-Domínguez, S. T. Ha, V. Valuckas, X. Liang, Y. Akimov, P. Bai, C. E. Png, H. V. Demir, A. I. Kuznetsov, *Laser Photonics Rev.* **2020**, *14*, 1900235.

- [23] S. T. Ha, Y. H. Fu, N. K. Emani, Z. Pan, R. M. Bakker, R. Paniagua-Domínguez, A. I. Kuznetsov, *Nat. Nanotechnol.* **2018**, *13*, 1042.
- [24] V. Mylnikov, S. T. Ha, Z. Pan, V. Valuckas, R. Paniagua-Domínguez, H. V. Demir, A. I. Kuznetsov, *ACS Nano* **2020**, *14*, 7338.
- [25] M. Wu, S. T. Ha, S. Shendre, E. G. Durmusoglu, W.-K. Koh, D. R. Abujetas, J. A. Sánchez-Gil, R. Paniagua-Domínguez, H. V. Demir, A. I. Kuznetsov, *Nano Lett.* **2020**, *20*, 6005.
- [26] A. Tripathi, H.-R. Kim, P. Tonkaev, S.-J. Lee, S. V. Makarov, S. S. Kruk, M. V. Rybin, H.-G. Park, Y. Kivshar, *Nano Lett.* **2021**, *21*, 6563.
- [27] M.-S. Hwang, H.-C. Lee, K.-H. Kim, K.-Y. Jeong, S.-H. Kwon, K. Koshelev, Y. Kivshar, H.-G. Park, *Nat. Commun.* **2021**, *12*, 4135.
- [28] M. Wu, L. Ding, R. P. Sabatini, L. K. Sagar, G. Bappi, R. Paniagua-Domínguez, E. H. Sargent, A. I. Kuznetsov, *Nano Lett.* **2021**, *21*, 9754.
- [29] F. Todisco, R. Malureanu, C. Wolff, P. Gonçalves, A. S. Roberts, N. A. Mortensen, C. Tserkezis, *Nanophotonics* **2020**, *9*, 803.
- [30] G. W. Castellanos, S. Murai, T. Raziman, S. Wang, M. Ramezani, A. G. Curto, J. Gómez Rivas, *ACS Photonics* **2020**, *7*, 1226.
- [31] R. Heilmann, A. I. Väkeväinen, J.-P. Martikainen, P. Törmä, *Nanophotonics* **2020**, *9*, 267.
- [32] M. Litinskaya, P. Reineker, V. M. Agranovich, *J. Lumin.* **2004**, *110*, 364.
- [33] N. Somaschi, L. Mouchliadis, D. Coles, I. Perakis, D. Lidzey, P. Lagoudakis, P. Savvidis, *Appl. Phys. Lett.* **2011**, *99*, 209.
- [34] D. M. Coles, P. Michetti, C. Clark, W. C. Tsoi, A. M. Adawi, J.-S. Kim, D. G. Lidzey, *Adv. Funct. Mater.* **2011**, *21*, 3691.
- [35] E. R. Bittner, S. Zaster, C. Silva, *arXiv:1206.2906*, **2012**.
- [36] L. Mazza, S. Kéna-Cohen, P. Michetti, G. C. La Rocca, *Phys. Rev. B* **2013**, *88*, 075321.
- [37] R. T. Grant, P. Michetti, A. J. Musser, P. Gregoire, T. Virgili, E. Vella, M. Cavazzini, K. Georgiou, F. Galeotti, C. Clark, J. Clark, C. Silva, D. G. Lidzey, *Adv. Opt. Mater.* **2016**, *4*, 1615.
- [38] G. Groenhof, C. Climent, J. Feist, D. Morozov, J. J. Toppari, *J. Phys. Chem. Lett.* **2019**, *10*, 5476.
- [39] J. M. Lüttgens, F. J. Berger, J. Zaumseil, *ACS Photonics* **2020**, *8*, 182.
- [40] Q. Zhao, J. Zhou, F. Zhang, D. Lippens, *Mater. Today* **2009**, *12*, 60.
- [41] A. E. Krasnok, A. E. Miroshnichenko, P. A. Belov, Y. S. Kivshar, *Opt. Express* **2012**, *20*, 20599.
- [42] I. Staude, A. E. Miroshnichenko, M. Decker, N. T. Fofang, S. Liu, E. Gonzales, J. Dominguez, T. S. Luk, D. N. Neshev, I. Brener, Y. Kivshar, *ACS Nano* **2013**, *7*, 7824.
- [43] V. G. Kravets, A. V. Kabashin, W. L. Barnes, A. N. Grigorenko, *Chem. Rev.* **2018**, *118*, 5912.
- [44] W. Wang, M. Ramezani, A. I. Väkeväinen, P. Törmä, J. G. Rivas, T. W. Odom, *Mater. Today* **2018**, *21*, 303.
- [45] V. E. Babicheva, J. V. Moloney, *Nanophotonics* **2018**, *7*, 1663.
- [46] K. Daskalakis, S. Maier, R. Murray, S. Kéna-Cohen, *Nat. Mater.* **2014**, *13*, 271.
- [47] T. Yagafarov, D. Sannikov, A. Zasedatelev, K. Georgiou, A. Baranikov, O. Kyriienko, I. Shelykh, L. Gai, Z. Shen, D. Lidzey, P. Lagoudakis, *Commun. Phys.* **2020**, *3*, 18.
- [48] G. H. Lodden, R. J. Holmes, *Phys. Rev. B* **2010**, *82*, 125317.
- [49] G. M. Akselrod, E. R. Young, M. S. Bradley, V. Bulović, *Opt. Express* **2013**, *21*, 12122.
- [50] T. Ishii, K. Miyata, M. Mamada, F. Bencheikh, F. Mathevet, K. Onda, S. Kéna-Cohen, C. Adachi, *Adv. Opt. Mater.* **2022**, *10*, 2102034.
- [51] D. Sannikov, T. Yagafarov, K. Georgiou, A. Zasedatelev, A. Baranikov, L. Gai, Z. Shen, D. Lidzey, P. Lagoudakis, *Adv. Opt. Mater.* **2019**, *7*, 1900163.
- [52] G. P. Agrawal, *Fiber-Optic Communication Systems*, John Wiley & Sons, Hoboken, NJ **2012**.
- [53] M. Ramezani, A. Halpin, S. Wang, M. Berghuis, J. G. Rivas, *Nano Lett.* **2019**, *19*, 8590.
- [54] A. Kodigala, T. Lepetit, Q. Gu, B. Bahari, Y. Fainman, B. Kanté, *Nature* **2017**, *541*, 196.
- [55] K. Koshelev, S. Sychev, Z. F. Sadrieva, A. A. Bogdanov, I. Iorsh, *Phys. Rev. B* **2018**, *98*, 161113.
- [56] V. Kravtsov, E. Khestanova, F. A. Benimetskiy, T. Ivanova, A. K. Samusev, I. S. Sinev, D. Pidgayko, A. M. Mozharov, I. S. Mukhin, M. S. Lozhkin, Y. V. Kapitonov, A. S. Brichkin, V. D. Kulakovskii, I. A. Shelykh, A. I. Tartakovskii, P. M. Walker, M. S. Skolnick, D. N. Krizhanovskii, I. V. Iorsh, *Light: Sci. Appl.* **2020**, *9*, 56.
- [57] V. Ardizzone, F. Riminucci, S. Zanotti, A. Gianfrate, M. Efthymiou-Tsironi, D. Suárez-Forero, F. Todisco, M. De Giorgi, D. Trypogeorgos, G. Gigli, K. Baldwin, L. Pfeiffer, D. Ballarini, H. S. Nguyen, D. Gerace, D. Sanvitto, *Nature* **2022**, *605*, 447.